Poynting Flux Input to the Auroral Ionosphere: The Impact of Subauroral Polarization Streams and Dawnside Auroral Polarization Streams

Jiang Liu[1,2], L. R. Lyons[2], Delores Knipp[3,4], Qiang Zhang[5], Chih-Ping Wang[2], Yangyang Shen[1], V. Angelopoulos[1], Yuzhang Ma[6], Sheng Tian[2], A. Artemyev[1], Chengyu Qian[7], Jun Liang[8], Hui Wang[7], and Ying Zou[9]

1. Department of Earth, Planetary, and Space Sciences, University of California, Los Angeles, USA.
2. Department of Atmospheric and Oceanic Sciences, University of California, Los Angeles, USA.
3. Smead Aerospace Engineering Science Department, University of Colorado, Boulder, USA
4. High Altitude Observatory, National Center for Atmospheric Research, Boulder, CO, USA
5. Tongji University, Shanghai, China
6. School of Space Science and Applied Physics, Shandong University, Weihai, China
7. Department of Space Physics, School of Electronic Information, Wuhan University, Hubei, China
8. Department of Physics and Astronomy, University of Calgary, Alberta, Canada
9. John Hopkins Applied Physics Laboratory, Laurel, Maryland, USA.

Key Points:

- We examine the distribution of Poynting flux into the ionosphere related to Joule heating using DMSP data with a novel gridding scheme.

- The highest Poynting flux is near the Region 1 and 2 currents' interface; the sunlit cusp also contains high Poynting flux.

- The Poynting flux is asymmetric about the R1/R2 interface, exhibiting distinct peaks in regions associated with SAPS and DAPS.

Abstract. The Poynting vector (Poynting flux) from Earth's magnetosphere downward towards its ionosphere carries the energy that powers the Joule heating in the ionosphere and thermosphere. The Joule heating controls fundamental ionospheric properties affecting the entire magnetosphere-ionosphere-thermosphere system, so it is necessary to understand when and where the Poynting flux is significant. Taking advantage of new datasets generated from DMSP (Defense Meteorological Satellite Program) observations, we investigate the Poynting flux distribution within and around the auroral zone, where most magnetosphere-ionosphere (M-I) dynamics and thus Joule heating occurs. We find that the Poynting flux, which is generally larger under more active conditions, is concentrated in the sunlit cusp and near the interface between Region 1 and 2 currents. The former concentration suggests voltage generators drive the cusp dynamics. The latter concentration shows asymmetries with respect to the interface between the Region 1 and 2 currents. We show that these reflect the controlling impact of subauroral polarization streams and dawnside auroral polarization streams on the Poynting flux.

Plain Language Summary

Earth's upper atmosphere and ionosphere receive energy from space in many ways, and one of them is through an incoming flux of electromagnetic energy. This is expressed as a 'Poynting flux', and we investigate how it is distributed in and around the ionosphere's auroral zone, where most activities occur. Our results show that large Poynting fluxes are distributed at locations where dramatic plasma flows appear, indicating a significant role of these flows in the energy circulation of the geospace.

1 Introduction

The heating of Earth's thermosphere and ionosphere modifies their temperature, composition, and conductivity (e.g., Farley et al., 1967; Hays et al., 1973; Aksnes et al., 2002), which are important aspects of space weather (e.g., Schunk & Sojka, 1996) impacting atmospheric and magnetospheric dynamics (e.g., Buonsanto et al., 1990; Wiltberger et al., 2004). One of the major heating forms is the Joule heating (e.g., Cole, 1962). It is often the dominant heating form at high latitudes (Vickrey et al., 1982; Lu et al., 1995), especially around the auroral zone (e.g., Knipp et al., 2004), the most active region of the ionosphere-thermosphere (I-T) system where dramatic events such as geomagnetic storms and substorms deposit their energy (e.g., Panov et al., 2016). The Joule heating in the I-T system is carried out by ionospheric electric fields and currents (e.g., Lu et al., 1995), both of which originate from magnetospheric processes and are modified by magnetosphere-ionosphere coupling (e.g., Vickrey et al., 1986). Thus, investigations of Joule heating can provide key information on the dynamic energy circulation between the magnetosphere, ionosphere, and thermosphere.

A direct investigation of the Joule heating requires measurements of electric fields and currents, which can only be obtained at limited altitudes by low-altitude spacecraft or within a limited field of view by radars (e.g., Kiene et al., 2019). To comprehensively investigate the Joule heating in a convenient way, Kelley et al. (1991) introduced an indirect approach based on the Poynting vector (also called Poynting flux) measured by low-altitude spacecraft:

$$S_{\mathrm{p}} = -(\mathbf{E} \times \delta\mathbf{B}) \cdot \hat{\mathbf{r}}/\mu_0, \quad (1)$$

where **E** is the electric field, expected to vanish during quiet (no plasma flow) times, $\delta\mathbf{B}$ is the magnetic field perturbation relative to Earth's main field, $\hat{\mathbf{r}}$ is the radial unit vector approximating the main field orientation, and S_{p} is the Poynting flux (approximately parallel to Earth's main field at high latitudes) associated with **E** and $\delta\mathbf{B}$. It is defined as positive when pointing from the magnetosphere downward towards the ground, which is almost always the case in the high latitude ionosphere, including the auroral zone (e.g., Gary et al., 1995; Knipp et al., 2021).

S_{p} contains contributions from perturbations of all frequencies, including those from quasi-steady dynamics such as the large-scale convection and those from waves (e.g., Billett et al., 2022). Under steady state conditions, S_{p} equals the total Joule heating rate of the entire unit column of ionosphere and thermosphere below the spacecraft (Kelley et al., 1991). This approximation assumes the neutral wind's modification to the Joule heating rate to be insignificant, which is usually valid at high latitudes where it is typically <15% (Billett et al., 2018). Under time-varying conditions, a part of S_p goes to particles via a parallel potential drop in the auroral acceleration region (e.g., Knight, 1973; Evans, 1974; Lyons, 1981). This part has been studied separately as associated with Alfvén waves (Wygant et al., 2000; Keiling et al., 2003) and comprises only a small portion of S_p (Janhunen et al., 2005). S_p may contain a contribution to the auroral acceleration region only when it is measured by a spacecraft above that region at ~2 R_E above the ground (Mozer & Hull, 2001), so for spacecraft at lower altitudes (as is the case for our study; see Section 2), S_p can well represent the Joule heating rate.

Recognizing the implications of S_p, previous studies have statistically investigated the global distributions of S_p to find where and how much electromagnetic energy is deposited to the ionosphere for Joule heating (Gary et al., 1995; Janhunen et al., 2005; Knipp et al., 2021). These studies showed that S_p is typically 1-10 mW/m^2 at ~300-1000 km altitude and larger during more active geomagnetic conditions (e.g., Billett et al., 2021). Large S_p values are concentrated in the cusp and auroral latitudes, as expected, since most magnetospheric activities map to these regions.

These previous studies, however, could not clarify the processes responsible for large S_p in the auroral zone, because they used magnetic latitudes to organize their statistics. The auroral zone and the various phenomena within it do not occur at constant latitudes, so their effects get intermingled when statistics are organized by latitude. These phenomena include subauroral polarization streams (SAPS), westward fast flows appearing equatorward of the bright electron aurora of the dusk convection cell (Foster & Vo, 2002), and dawnside auroral polarization streams (DAPS), eastward fast flows appearing poleward of the bright arc of the dawn convection cell (Liu et al., 2020). Both streams result from enhanced convection involving mesoscale magnetospheric processes (e.g., Gallardo-Lacourt et al., 2017) and can lead to significant Joule heating (Wang et al., 2011; Zou et al., 2013). Despite these previous findings, the extent and significance of the streams' Joule heating in the context of the global-scale auroral zone are still unclear.

To investigate the role of dynamic phenomena such as SAPS and DAPS in the energy budget of the auroral zone, we study the statistical distribution of S_p after organizing it in physical grids representing locations relative to the Region 1 and 2 (R1 and R2) currents (Iijima & Potemra, 1976), the field-aligned currents (FACs) implicated in the large-scale M-I convection (e.g., Tanaka, 1995). The Region 1 current occupies the higher latitude part of the auroral oval; its magnetospheric origin includes the higher latitude plasma sheet and the plasma sheet boundary layer. The Region 2 current covers the lower latitude part of the oval, which maps to the central plasma sheet and the inner magnetosphere (e.g., Ohtani et al., 1988; Liu et al., 2016). The locations of the R1 and R2 currents are known to determine those of SAPS and DAPS (e. g., Anderson et al., 1993; Liu et al., 2020) and organize other ionospheric phenomena. Our study involving these currents' locations is made possible by two newly available datasets.

2 Datasets

Our investigation is based on a recently assembled S_p database (Knipp et al., 2021) and a recent method for determining boundaries of Region 1 and 2 currents (Liu et al., 2022), both using data from the DMSP mission. All DMSP spacecraft are polar orbiting with a low-earth orbit of ~850 km altitude.

The Poynting flux S_p has been computed using Equation 1, where the perturbation magnetic field comes from DMSP's fluxgate magnetometer (Rich, 1984) and the electric field is inferred from $\mathbf{E} = -\mathbf{v} \times \mathbf{B}_0$ (the corotation electric field has been subtracted; see Kilcommons et al. (2022)). Here $\mathbf{B}_0$ is the International Geomagnetic Reference Field and $\mathbf{v}$ is the ion bulk flow in the Earth frame (satellite velocity has been subtracted). Unlike most previous DMSP studies of the Poynting flux which only used the cross-track components of $\mathbf{v}$ (e.g., Knipp et al., 2011; Huang et al., 2017), the bulk flow here includes all components measured by the Ion Drift Meter and the Retarding Potential Analyzer of DMSP with the newest quality flags (Hairston & Coley, 2019). Knipp et al. (2021) provide more information about this S_p dataset, which is available for DMSP-f15, f16, and f18 for the years 2011-2014. This availability range marks the scope of our statistical studies.

The other dataset we use is boundaries of R1 and R2 currents identified from DMSP transects of the auroral zone. Liu et al. (2022) determined these boundaries using a fully-automated algorithm based on the perturbation magnetic field. This algorithm has been applied to all DMSP auroral zone transects with the available Poynting flux data (Knipp et al., 2021), which provide 14796 transects with R1 and R2 boundaries thus identified for our statistical studies (as illustrated in Figure 1).

3 Results

We examine the Poynting flux distribution within and around the auroral zone by generating statistical maps. These maps will contain many longitudinal and latitudinal bins to reveal detailed S_p distribution. We define the longitudinal bins as evenly distributed magnetic local time (MLT) bins. For the latitudinal bins, we use a novel and more physical definition—we construct them regarding the ranges of Region 1 and 2 currents. The details in these ranges will be represented by several latitudinal bins within each range. Because the latitudinal widths of the R1 and R2 currents are different for different auroral zone transects of DMSP, dividing them into fixed-width latitudinal bins would result in different numbers of bins for different transects, prohibiting the assembly of data from many transects to generate statistical distributions. Thus, we divide each of the R1 and R2 ranges into a fixed number of bins. This is done by segmenting the spacecraft trajectory of each DMSP transect regarding the widths of the observed R1 and R2 ranges, as illustrated in Figure 2.

For each transect, we define three magnetic latitudes of boundary locations: Λ_1, the poleward boundary of the R1 current, Λ_{12}, the interface between the R1 and R2 current, and Λ_2, the equatorward boundary of the R2 current. By definition, $|\Lambda_1|>|\Lambda_{12}|>|\Lambda_2|$. We divide the R1 range, which has a latitudinal width of $\Delta\Lambda_1=|\Lambda_1-\Lambda_{12}|$, into three segments, each with the same latitudinal width of $\Delta\Lambda_1/3$. We do the same to the R2 range (latitudinal width: $\Delta\Lambda_2=|\Lambda_{12}-\Lambda_2|$) and get three segments with a width of $\Delta\Lambda_2/3$ for each. (Note that Λ_{12} is not contained by any of the segments.) We also identify the three consecutive segments immediately poleward of the R1 current, each with a latitudinal width of $\Delta\Lambda_1/3$, and one segment immediately equatorward of the R2 current with a width of $\Delta\Lambda_2/3$. These additional segments will provide useful information beyond the auroral oval. Now we have ten segments for each auroral zone transect of DMSP. For every segment, we designate the average values of quantities (e.g., S_p and MLT) over it as its signature values. Using the signature values of the segments from all DMSP transects in our database (regardless of northern or southern hemisphere), we construct statistical maps of different quantities in the following. Please note that these maps cannot be perceived in the same way as traditional maps (i.e., those using actual latitudes as grids) because the signature values on the two sides of the R1/R2 interface are averages over different latitudinal widths. Nevertheless, they are no less meaningful than averages over the same widths because M-I dynamics are not expected to be better prescribed by absolute latitude widths than by those normalized by the R1 or R2 width.

Figure 3 presents statistical maps of S_p. To investigate how the Poynting flux depends on geomagnetic activity levels, we split the dataset into quiet conditions defined as Kp<3 (Figures 3a-3b) and active conditions defined as Kp≥3 (Figures 3c-3d). We chose Kp to represent the activity level following previous statistical studies on Poynting flux (Olsson et al., 2004; Knipp et al., 2021) so our results can be conveniently compared with theirs. We also separate the results for sunlit (Figures 3a and 3c) and dark (Figures 3b and 3d) conditions because they are known to impact the Poynting flux via their different ionospheric conductivities due to different levels of solar EUV ionization (e.g., Pakhotin et al., 2021). We determined these conditions for each transect segment using the signature location and time of that segment; the criterion for sunrise/sunset is $90^{o}50'$

solar zenith angle (Jacobson et al., 2011). Separating the segments based on their sunlit condition allows us to mix the data from northern and southern hemispheres together for our statistical study. For the segments in each statistical subset, we position them in different bins (colored arc areas in Figure 3) based on their relative location to the R1/R2 current and signature MLT values. For each bin, we compute the median of the signature S_p of all the segments in that bin. These medians, as represented by the bin colors, reveal typical distributions of Poynting flux input to the ionosphere. To assure the quality of the statistical results, we show the medians only for bins containing segments from ≥30 DMSP transects. Such bins are most abundant near the dawn and dusk sectors because of DMSP's sun-synchronous orbits around the dawn-dusk meridian, but there are also a few bins satisfying the quality criterion in the noon and midnight sectors.

The S_p distributions reveal that their median values are always downward (towards the ground) and typically 1-10 mW/m^2. In general, the ionosphere receives significantly higher Poynting flux during active times (with typical values up to >10 mW/m^2, as given by the medians in Figures 3c-3d) than during quiet times (<5 mW/m^2; Figures 3a-3b). These values under various conditions are consistent with previous findings (e.g., Knipp et al., 2021). Regardless of the condition or MLT, S_p peaks in the bins adjacent to the R1/R2 interface and decreases away from it until it approaches zero in the bins immediately equatorward of the R1 current's poleward boundary and in the bins immediately poleward of the R2 current's equatorward boundary. Equatorward of the R2 current, the Poynting flux is negligible. Poleward of the R1 current, S_p is typically <3 mW/m^2, but can be significant (>5 mW/m^2) near the noon meridian under sunlight

(Figures 3a and 3c). Between 8 and 14 MLT during active and sunlit conditions (Figure 3c), S_p is ~ 5 mW/m^2 poleward of the R1 current. This region is the cusp (e.g., Jacobsen et al., 2010) and has been shown to contain high Poynting flux (e.g., Cosgrove et al., 2014).

Taking a closer look at Figure 3, we find an interesting feature: S_p is usually asymmetrically distributed about the R1/R2 interface. In most MLT bins (13 out of 18) from postnoon to premidnight, S_p in the bins equatorward of the interface are larger than those poleward of it with the same normalized distances to it, so the maximum S_p occurs in the bins immediately equatorward of the interface. During active times (Figures 3c-3d), this difference is typically >50%. From postmidnight to prenoon, an opposite asymmetry shows up under darkness (Figures 3b and 3d): at any given MLT, S_p peaks in the bin immediately poleward of the R1/R2 interface and is significantly larger (>30% under quiet conditions and >50% under active conditions) than that in the bin immediately equatorward of the interface.

3.1 Factors Contributing to the Poynting Flux Distribution

To find what leads to the distributions in Figure 3, we examine the factors contributing to the Poynting flux. Converting Equation 1 into scalar form:

$$S_{\mathrm{p}} = -[(\mathbf{E}_h + \mathbf{E}_r) \times (\delta\mathbf{B}_h + \delta\mathbf{B}_r)] \cdot \frac{\hat{\mathbf{r}}}{\mu_0} = -(\mathbf{E}_h \times \delta\mathbf{B}_h) \cdot \frac{\hat{\mathbf{r}}}{\mu_0} = -E_h \delta B_h \sin\theta_{\mathrm{BE}} / \mu_0,$$

Where suffices *h* and *r* indicate the horizontal (to earth surface) and radial components, respectively. It is evident that S_p should be proportional to the magnitudes of the horizontal electric and perturbation magnetic fields E_h and δB_h and $\sin\vartheta_{BE}$, where ϑ_{BE} is the angle between $\mathbf{E}_h$ and $\delta\mathbf{B}_h$. Figure 4 shows the distribution of these factors, with the horizontal ion bulk flow v_h as the proxy of E_h ($\mathbf{E}_\mathrm{h} \approx -\mathbf{v}_h \times \mathbf{B}_0$; $\mathbf{B}_0$ is the nearly vertical main field). As indicated by Figures 4a-4h, the higher Poynting flux during active times is caused by larger plasma flows and perturbation magnetic fields. The flows (Figures 4a-4d; and thus electric field) are also higher under darkness than under sunlight, as expected from 'current generators' in the magnetosphere (Vickrey et al., 1986). On the contrary, $\delta\mathbf{B}_h$ (Figures 4e-4h) presents an opposite dependence on illumination, although it does not dominate the Poynting flux's dependence. According to Ampere's law, this $\delta\mathbf{B}_h$ dependence indicates that field-aligned currents are more intense under sunlight than under darkness. Current continuity requires the same for horizontal ionospheric currents, which suggests 'voltage generators' as their magnetospheric sources (Vickrey et al., 1986). $\delta\mathbf{B}_h$ and $\mathbf{E}_h$ are more perpendicular to each other (higher $\sin\vartheta_{BE}$ in Figures 4i-4l) under sunlight than under darkness, but this does not affect the Poynting flux's dependence on illumination significant enough to overturn it.

The high S_p near the R1/R2 interface is contributed by all factors—v_h, δB_h, and $\sin\vartheta_{BE}$ all peak near the interface and decrease away from it. All factors also contribute to the high Poynting flux in the sunlit cusp (Figures 4a, 4c, 4e, 4g, 4i, and 4k). Although the dark cusp and polar cap contain significant flows (>0.5 km/s; Figures 4b and 4d), the lack of magnetic perturbations there (Figures 4f and 4h) leads to small S_p. Equatorward of the R2 current, vanishing magnetic field perturbations (Figures 4e-4h) lead to vanishing S_p.

Details in Figure 4 reveal the contributors to the asymmetry in the S_p distribution about the R1/R2 interface. While the magnetic field perturbation contributes to the asymmetry only for the active-time postnoon-to-premidnight sector as in Figures 4g-4h,

$\sin\vartheta_{BE}$ and plasma flows always contribute to it—they are larger in the R2 range than in the R1 range in the postnoon-to-premidnight sector; they are larger in the R1 range than in the R2 range in the postmidnight-to-prenoon sector. The peak plasma flows equatorward of the R1/R2 interface in the postnoon-to-premidnight sector are at where subauroral polarization streams are expected, and the peak flows poleward of the interface in the postmidnight-to-prenoon sector should be contributed by dawnside auroral polarization streams. In the postmidnight-to-prenoon sector, the difference in flow magnitude across the interface is much larger under dark conditions than under sunlit conditions (Figures 4a-4d), consistent with the DAPS generation mechanism suggested by Liu et al. (2020). This is a major factor leading to the difference in the S_p asymmetry about the R1/R2 interface between sunlit (Figures 3a and 3c) and dark (Figures 3b and 3d) conditions in the postmidnight-to-prenoon sector.

3.2 The Role of SAPS and DAPS

Figures 4a-4d suggest that SAPS and DAPS may contribute to the Poynting flux asymmetry about the R1/R2 interface. To evaluate this idea, we examine typical DMSP observations of SAPS (Figures 5a-5d) and DAPS (Figures 5e-5g). A SAPS is a fast westward flow (Figure 5b) equatorward of the electron aurora as indicated by electron precipitations (Figure 5d). At the same location of the SAPS is an enhanced downward Poynting flux (Figure 5c). To put this region into the context of the auroral zone, we determine the ranges of R1 and R2 currents based on the gradual slopes of the magnetic field's east-west component, as marked in Figure 5a (see, e.g., Liu et al., 2021 for this method). The high Poynting flux is equatorward of the R1/R2 interface and much larger than that poleward of it, consistent with the statistical asymmetries in the postnoon-to-premidnight sector of Figure 3. Figure 5f shows a typical DAPS, an eastward fast flow in the dawn convection cell (as indicated by the R1 and R2 FAC directions in Figure 3e) near the R1/R2 interface. A typical signature of DAPS is that the eastward flow poleward of the interface is much larger than that equatorward of it, which causes the same asymmetry in Poynting flux (Figure 5g). This asymmetry is consistent with those in the postmidnight-to-prenoon sector of Figures 3b and 3d.

To better illustrate the streams' impact on the Poynting flux distribution, in Figure 6 we generate a statistical S_p map from the DMSP transects with either SAPS or DAPS observed. We identified SAPS and DAPS using fully automated algorithms (Appendix A), which gave us 2028 and 1301 transects with SAPS and DAPS, respectively. The locations of these transects are indicated by green and red dots in Figure 1. Because SAPS and DAPS are themselves condition-dependent, we no longer divide these transects into subgroups based on activity level or illumination. Figure 6 shows the S_p asymmetries more clearly than any panel in Figure 3: In the postnoon-to-premidnight sector, S_p immediately equatorward of the R1/R2 interface is much larger than poleward of the interface; in the postmidnight-to-prenoon sector, S_p immediately poleward of the R1/R2 interface is much larger than equatorward of the interface.

4 Conclusion and Discussion

Our statistical results have revealed the following:

1. The Poynting flux input to the ionosphere (as computed from Equation 1) is higher during active times than during quiet times, consistent with previous findings (e.g., Gary et al., 1995; Cosgrove et al., 2014; Kaeppler et al., 2022).
2. Under all activity and illumination conditions, the highest Poynting flux input occurs near the interface between Region 1 and 2 currents and decreases toward the poleward and equatorward boundaries of the R1 and R2 current, respectively. Such a distribution is caused by all factors contributing to the Poynting flux: near the interface, the plasma bulk flow (and thus electric field) and the perturbation magnetic field are larger than in other places; the angle between the electric and the perturbation magnetic fields is closer to 90^o. These flow and magnetic field peaks are consistent with the typical convection profile in the auroral zone (Archer et al., 2017).
3. The sunlit cusp is another region of high Poynting flux input, especially during active times. In contrast, the dark cusp does not show a concentration of Poynting flux, although its plasma flows are as intense as those in the sunlit cusp. This controlling factor of the Poynting flux in the cusp is the perturbation magnetic field, which is much larger in the sunlit cusp than in the dark cusp. The magnetic perturbations are caused by field-aligned currents, which must be connected to horizontal ionospheric currents to ensure current continuity. Therefore, the difference in magnetic perturbations between the sunlit and dark cusp indicates a difference in horizontal ionospheric currents, which is most likely related to the ionospheric conductivity—the higher conductivity under sunlit

conditions allows larger horizontal current, and thus FACs, magnetic perturbations, and Poynting flux. This role of the conductivity reveals that the magnetospheric sources of the cusp's dynamic processes are 'voltage generators' instead of 'current generators' (see e.g., Lysak, 1985; Vickrey et al., 1986 for the meanings of these terms)—the processes originate as potential electric fields instead of currents needing closure through the ionosphere. Such voltage generators can cause significant Poynting flux only in regions of high ionospheric conductivity.

4. The Poynting flux shows asymmetries about the R1/R2 interface—in the postnoon-to-premidnight sector of the R1 and R2 range, the Poynting flux equatorward of the interface is significantly higher (~30% to >50% in statistical medians) than that poleward of it; in the postmidnight-to-prenoon sector, the asymmetry is opposite. The asymmetries are more prominent if we only include DMSP transects observing SAPS or DAPS in the statistics (Figure 3i), suggesting that these streams are responsible for the asymmetries. Confirming this notion, plasma flows are a major contributor to the asymmetries (Figures 4a-4d). The asymmetry in the postnoon-to-premidnight sector exists under all conditions but that in the postmidnight-to-prenoon sector only shows up under darkness. This difference suggests that the generation of DAPS depends on conductivity much more than that of SAPS. As Liu et al. (2020) suggested, an auroral zone conductivity gradient caused by precipitation is crucial for prominent DAPS signatures, but this gradient can be much suppressed under sunlight. The

Poynting flux equatorward of the R1/R2 interface in the postmidnight sector receives limited contributions from abnormal SAPS (Voiculescu & Roth, 2008; D. Lin et al., 2022), which are less common and slower than DAPS (Qian & Wang, 2023).

All these signatures of the Poynting flux distribution also show up in statistical quartiles (Figures S1-S4 in the supporting information), so they are robust results.

The conclusions above come from DMSP data, which were measured at ~850 km altitude. Thus, the investigated Poynting flux does not contribute to the auroral acceleration region (see Section 1) and should mostly become Joule heating in the ionosphere and thermosphere. The conclusions about the Poynting flux' distribution and asymmetries may also be applied to Joule heating. For example, the asymmetries about the R1/R2 interface (Point 4 above) indicate strong Joule heating and thus recombination in the R2 range of the postnoon-to-premidnight sector and the R1 range of the postmidnight-to-prenoon sector. The recombination may cause low density troughs to form in these two regions, consistent with observations (e.g., Anderson et al., 1991; Zou et al., 2013). The Joule heating may also lead to phenomena such as the STEVE (Strong Thermal Emission Velocity Enhancement; MacDonald et al., 2018), which has received intense research focus recently (Harding et al., 2020). Our results provide important information for predicting such phenomena.

Appendix A: Selection Algorithms for SAPS and DAPS

We look for SAPS and DAPS by applying fully automated algorithms (including all the following) to the DMSP auroral zone transects used for our Poynting flux statistics, which all have identified R1 and R2 ranges (see Section 2). As a preparation, from the magnetic field slopes within the R1 and R2 ranges we automatedly determine the directions of the R1 and R2 FACs (e.g., Figure 5e). These directions indicate which convection cell the spacecraft transected–the dusk cell is given by an upward R1 FAC and the dawn cell by a downward R1 FAC. This method is more accurate than using spacecraft ephemerides because the convection cells do not stay at constant locations (see Walach et al., 2022 and references therein). We select SAPS and DAPS only from the dusk and dawn convection cells, respectively, as consistent with their definitions.

We select SAPS and DAPS from DMSP's cross-track flow measurements, which we treat as (approximately) east-west flows. We smooth the original measurements v_{cross} using the Kitagawa (1981) method with a half bandwidth equal to the inverse of the total latitudinal width of the R1 and R2 currents. The goal of this smoothing is to remove secondary flow variations that may confuse the selection for SAPS and DAPS.

A.1 SAPS Selection

A SAPS is defined as a significant westward flow equatorward of the prominent electron aurora in the dusk convection cell (e.g., C. S. Lin & Hoffman, 1982). Thus, we first need to find the equatorward boundary of the electron aurora from each DMSP transect of the dusk convection cell. Because electron aurora intensity is proportional to ionospheric conductance (Lam et al., 2019; Gabrielse et al., 2021), we look for the aurora boundary based on Σ_{P}, the Pederson conductance. This is a common practice for identifying aurora boundaries from DMSP observations (e.g., Wang et al., 2008). After computing Σ_{P} from electron precipitation using the Robinson et al. (1987) equation, we smooth it to get $\widetilde{\Sigma_{\mathrm{P}}}$ (the third row from top of Figure A1) using the same method applied to the cross-track flow. Next, we characterize the auroral zone using Λ_{M}, the latitudinal location of the maximum $\widetilde{\Sigma_{\mathrm{P}}}$ in the Region 1 and 2 range, and $\widehat{\widetilde{\Sigma_{\mathrm{P}}}}_{\mathrm{Au}}$, the overall auroral brightness of each DMSP transect, which is computed as the average $\widetilde{\Sigma_{\mathrm{P}}}$ over the expected overall range of auroral emissions. By default, we use the R1 range for this range, because the R1 current in the dusk convection cell is an upward FAC carried by precipitating electrons producing auroral emissions. However, the range of bright auroral emissions is not always collocated with the R1 current (Carter et al., 2016), so Λ_{M} sometimes falls outside the R1 current (then it must be within the R2 range). Under such conditions, we extend the averaging range to be from Λ_{M} to the poleward boundary of the R1 current to include the significant auroral precipitation in the R2 range.

Next, we divide the time interval of the DMSP track between Λ_{M} and the equatorward boundary of the R2 current (Λ_2) into *N* equally spaced windows. *N* is chosen as follows: if the whole interval is >50 seconds, *N*=10; otherwise, *N* is the maximum integer allowing each window to be ≥5 seconds. Next, we identify the poleward-most window with every window equatorward of it (including itself) having an average $\widetilde{\Sigma_{\mathrm{P}}}$ smaller than $0.2\widehat{\widetilde{\Sigma_{\mathrm{P}}}}_{\mathrm{Au}}$ or 1 mho (the criterion values come from Wang et al. (2008)). If such a window can be identified (W_{Low}), we look for the equatorward boundary of the electron auroral within this window by dividing it into *n* small time windows—*n* is the smallest integer allowing each resultant window to be ≤5 seconds. We then repeat what we did to the *N* windows above to these *n* small windows to identify a final low-conductance small window. If such a small window can be identified, we take its poleward boundary as Λ_{AU}, the equatorward boundary of the electron aurora. Otherwise, we define Λ_{AU} as the equatorward boundary of W_{Low}. Figure A1 illustrates examples of identified Λ_{AU} (orange dotted lines).

For SAPS selection, we first identify all westward peaks of the smoothed flow $\tilde{v}_{cross}$ within the range equatorward of Λ_{AU} and poleward of Λ_2. The generation mechanism of SAPS requires it to be within this range (e.g., Anderson et al., 1993). For all the locations of identified $\tilde{v}_{cross}$ peaks, we examine whether their original v_{cross} is at least 0.5 km/s larger than v_{cross}^{q}, the flow in the unperturbed region (determined as the average of the 30 seconds of data immediately equatorward of the R2 range). We chose the 0.5 km/s criterion following Zhang et al. (2020). Of the peaks satisfying this criterion (if any), we select the one with the largest $\tilde{v}_{cross}$ as the SAPS peak. Figure A1 shows examples of selected SAPS (with their peaks indicated by dotted magenta lines).

A.2 DAPS Selection

Our DAPS selection algorithm is designed based on the typical events reported by Liu et al. (2020). First, we compute an average-sense eastward flow gradient as $K_0 = \left(\tilde{v}_{cross}^{E,\mathrm{max}} - v_{cross}^{\mathrm{q}}\right)/\Delta\Lambda_2$, where $\tilde{v}_{cross}^{E,\mathrm{max}}$ is the maximum eastward flow of the R1 and R2 range. Next, within the range between $\Lambda_{12} - \Delta\Lambda_2/3$ and $\Lambda_{12} + \Delta\Lambda_1/3$, we find all data points of $d\tilde{v}_{cross}/d|\Lambda|$ with the same sign as K_0 and a magnitude exceeding $3|K_0|$, where Λ is the magnetic latitude. Each continuous group of such data points (if they exist) is regarded as a significant eastward flow gradient. For each significant gradient, we examine the range immediately poleward of it with a latitudinal width of $0.3\Delta\Lambda_1$ (if this range's poleward edge is poleward of the R1 current's poleward boundary, we adjust it to be that poleward boundary) and the one immediately equatorward of it with a width of $0.3\Delta\Lambda_2$ (if this range's equatorward edge is equatorward of the R2 current's equatorward boundary, we adjust it to that equatorward boundary). If the maximum eastward v_{cross} of the former range is larger than that of the latter range and v_{cross}^{q} by ≥0.5 km/s, we mark this gradient as a candidate for final selection. Of all candidates, we select the one with its poleward edge closest to the R1/R2 interface as that of a DAPS and define the eastward flow poleward of it as a DAPS. Figure A2 shows examples of selected DAPS.

Acknowledgements. We thank James McTiernan for help with figure plotting, Roger Varney for useful discussions, and the DMSP team for producing data. The work at UCLA was supported by NASA grants 80NSSC23K0903, 80NSSC22K0749, 80NSSC22K0751, 80NSSC22K1012, 80NSSC20K1314, and contract NAS5-02099 and NSF grants AGS-2055192, AGS-2247034, and AGS-2224108. DJK was partially supported by AFOSR Award FA9550-17-1-0258. YZ was supported by NSF grant AGS-2405261 and NASA grant 80NSSC21K0729.

Open Research/Data Availability Statement

The data used in this study are publicly available at the Madrigal site (http://cedar.openmadrigal.org/) and the National Centers for Environmental

Information (https://www.ngdc.noaa.gov/stp/geomag/kp_ap.html). To access the DMSP data in the Madrigal site, please go to http://cedar.openmadrigal.org/single and then from the drop down menus select ‘Satellite Instruments’ -> ‘Defense Meteorological Satellite Program’ -> Year -> Month -> Date -> Select experiment. All the DMSP datafiles for the selected date will show up on the page. The software employed in this study is available at the SPEDAS software page https://themis.ssl.berkeley.edu/software.shtml and Zenodo (https://zenodo.org/records/11176127).

References

Aksnes, A., Stadsnes, J., Bjordal, J., Østgaard, N., Vondrak, R. R., Detrick, D. L., et al. (2002). Instantaneous ionospheric global conductance maps during an isolated substorm. *Annales Geophysicae*, *20*(8), 1181–1191. https://doi.org/10.5194/angeo-20-1181-2002

Anderson, P. C., Heelis, R. A., & Hanson, W. B. (1991). The ionospheric signatures of rapid subauroral ion drifts. *Journal of Geophysical Research*, *96*(A4). https://doi.org/10.1029/90ja02651

Anderson, P. C., Hanson, W. B., Heelis, R. A., Craven, J. D., Baker, D. N., & Frank, L. A. (1993). A proposed production model of rapid subauroral ion drifts and their relationship to substorm evolution. *Journal of Geophysical Research: Space Physics*, *98*(A4), 6069–6078. https://doi.org/10.1029/92ja01975

Archer, W. E., Knudsen, D. J., Burchill, J. K., Jackel, B., Donovan, E., Connors, M., & Juusola, L. (2017). Birkeland current boundary flows. *Journal of Geophysical Research: Space Physics*, *122*(4), 4617–4627. https://doi.org/10.1002/2016ja023789

Billett, D. D., Grocott, A., Wild, J. A., Walach, M.-T., & Kosch, M. J. (2018). Diurnal Variations in Global Joule Heating Morphology and Magnitude Due To Neutral Winds. *Journal of Geophysical Research: Space Physics*. https://doi.org/10.1002/2017JA025141

Billett, D. D., Perry, G. W., Clausen, L. B. N., Archer, W. E., McWilliams, K. A., Haaland, S., et al. (2021). The Relationship Between Large Scale Thermospheric Density Enhancements and the Spatial Distribution of Poynting Flux. *Journal of Geophysical Research: Space Physics*, *126*(5), e2021JA029205. https://doi.org/10.1029/2021JA029205

Billett, D. D., McWilliams, K. A., Pakhotin, I. P., Burchill, J. K., Knudsen, D. J., & Martin, C. J. (2022). High-Resolution Poynting Flux Statistics From the Swarm Mission: How Much Is Being Underestimated at Larger Scales? *Journal of Geophysical Research: Space Physics*, *127*(7), e2022JA030573. https://doi.org/10.1029/2022JA030573

Buonsanto, M. J., Foster, J. C., Galasso, A. D., Sipler, D. P., & Holt, J. M. (1990). Neutral winds and thermosphere/ionosphere coupling and energetics during the geomagnetic disturbances of March 6–10, 1989. *Journal of Geophysical Research*, *95*(A12), 21033. https://doi.org/10.1029/JA095iA12p21033

Carter, J. A., Milan, S. E., Coxon, J. C., Walach, M. -T., & Anderson, B. J. (2016). Average field-aligned current configuration parameterized by solar wind conditions. *Journal of Geophysical Research: Space Physics*, *121*(2), 1294–1307. https://doi.org/10.1002/2015JA021567

Cole, K. D. (1962). Joule Heating of the Upper Atmosphere. *Australian Journal of Physics*, *15*(2), 223. https://doi.org/10.1071/PH620223

Cosgrove, R. B., Bahcivan, H., Chen, S., Strangeway, R. J., Ortega, J., Alhassan, M., et al. (2014). Empirical model of Poynting flux derived from FAST data and a cusp signature. *Journal of*

Geophysical Research: Space Physics, *119*(1), 411–430. https://doi.org/10.1002/2013JA019105

Evans, D. S. (1974). Precipitating electron fluxes formed by a magnetic field aligned potential difference. *Journal of Geophysical Research*, *79*(19), 2853–2858. https://doi.org/10.1029/JA079i019p02853

Farley, D. T., McClure, J. P., Sterling, D. L., & Green, J. L. (1967). Temperature and composition of the equatorial ionosphere. *Journal of Geophysical Research*, *72*(23), 5837–5851. https://doi.org/10.1029/JZ072i023p05837

Foster, J. C., & Vo, H. B. (2002). Average characteristics and activity dependence of the subauroral polarization stream. *Journal of Geophysical Research: Space Physics*, *107*(A12), SIA 16-1-SIA 16-10. https://doi.org/10.1029/2002ja009409

Gabrielse, C., Nishimura, T., Chen, M., Hecht, J. H., Kaeppler, S. R., Gillies, D. M., et al. (2021). Estimating Precipitating Energy Flux, Average Energy, and Hall Auroral Conductance From THEMIS All-Sky-Imagers With Focus on Mesoscales. *Frontiers in Physics*, *9*, 744298. https://doi.org/10.3389/fphy.2021.744298

Gallardo-Lacourt, B., Nishimura, Y., Lyons, L. R., Mishin, E. V., Ruohoniemi, J. M., Donovan, E. F., et al. (2017). Influence of Auroral Streamers on Rapid Evolution of Ionospheric SAPS Flows. *Journal of Geophysical Research: Space Physics*, *122*(12), 12,406-12,420. https://doi.org/10.1002/2017ja024198

Gary, J. B., Heelis, R. A., & Thayer, J. P. (1995). Summary of field-aligned Poynting flux observations from DE 2. *Geophysical Research Letters*, *22*(14), 1861–1864. https://doi.org/10.1029/95GL00570

Hairston, M., & Coley, W. R. (2019). A Short Introduction to the DMSP SSIES-3 Quality Flags and How to Use Them (Version version 1). https://doi.org/10.5281/ZENODO.4776161

Harding, B. J., Mende, S. B., Triplett, C. C., & Wu, Y. J. (2020). A Mechanism for the STEVE Continuum Emission. *Geophysical Research Letters*, *47*(7), e2020GL087102. https://doi.org/10.1029/2020GL087102

Hays, P. B., Jones, R. A., & Rees, M. H. (1973). Auroral heating and the composition of the neutral atmosphere. *Planetary and Space Science*, *21*(4), 559–573. https://doi.org/10.1016/0032-0633(73)90070-6

Huang, C. Y., Huang, Y., Su, Y.-J., Hairston, M. R., & Sotirelis, T. (2017). DMSP observations of high latitude Poynting flux during magnetic storms. *Journal of Atmospheric and Solar-Terrestrial Physics*, *164*, 294–307. https://doi.org/10.1016/j.jastp.2017.09.005

Iijima, T., & Potemra, T. A. (1976). The amplitude distribution of field-aligned currents at northern high latitudes observed by Triad. *Journal of Geophysical Research*, *81*(13), 2165–2174. https://doi.org/10.1029/JA081i013p02165

Jacobsen, K. S., Moen, J. I., & Pedersen, A. (2010). Quasistatic electric field structures and field-aligned currents in the polar cusp region. *Journal of Geophysical Research: Space Physics*, *115*(A10), 2010JA015467. https://doi.org/10.1029/2010JA015467

Jacobson, L. D., Seaver, A., & Tang, J. (2011). AstroCalc4R : software to calculate solar zenith angle; time at sunrise, local noon, and sunset; and photosynthetically available radiation based on date, time, and location. U.S. Department of Commerce, Northeast Fish Sci Cent RefDoc. Retrieved from https://repository.library.noaa.gov/view/noaa/3867

Janhunen, P., Olsson, A., Tsyganenko, N. A., Russell, C. T., Laakso, H., & Blomberg, L. G. (2005). Statistics of a parallel Poynting vector in the auroral zone as a function of altitude using Polar EFI and MFE data and Astrid-2 EMMA data. *Annales Geophysicae*, *23*(5), 1797–1806. https://doi.org/10.5194/angeo-23-1797-2005

Kaeppler, S. R., Knipp, D. J., Verkhoglyadova, O. P., Kilcommons, L. M., & Zhan, W. (2022). Electromagnetic energy input and dissipation. In *Cross-Scale Coupling and Energy Transfer in the Magnetosphere-Ionosphere-Thermosphere System* (pp. 301–355). Elsevier. https://doi.org/10.1016/B978-0-12-821366-7.00006-8

Keiling, A., Wygant, J. R., Cattell, C. A., Mozer, F. S., & Russell, C. T. (2003). The Global Morphology of Wave Poynting Flux: Powering the Aurora. *Science*, *299*(5605), 383–386. https://doi.org/10.1126/science.1080073

Kelley, M. C., Knudsen, D. J., & Vickrey, J. F. (1991). Poynting flux measurements on a satellite: A diagnostic tool for space research. *Journal of Geophysical Research*, *96*(A1), 201. https://doi.org/10.1029/90JA01837

Kiene, A., Bristow, W. A., Conde, M. G., & Hampton, D. L. (2019). High-Resolution Local Measurements of *F* Region Ion Temperatures and Joule Heating Rates Using SuperDARN and Ground-Based Optics. *Journal of Geophysical Research: Space Physics*, *124*(1), 557–572. https://doi.org/10.1029/2018JA025997

Kilcommons, L. M., Knipp, D. J., Hairston, M., & Coley, W. R. (2022). DMSP Poynting Flux: Data Processing and Inter-Spacecraft Comparisons. *Journal of Geophysical Research: Space Physics*, *127*(8), e2022JA030299. https://doi.org/10.1029/2022JA030299

Kitagawa, G. (1981). A Nonstationary Time Series Model and Its Fitting by a Recursive Filter. *Journal of Time Series Analysis*, *2*(2), 103–116. https://doi.org/10.1111/j.1467-9892.1981.tb00316.x

Knight, S. (1973). Parallel electric fields. *Planetary and Space Science*, *21*(5), 741–750. https://doi.org/10.1016/0032-0633(73)90093-7

Knipp, D. J., Tobiska, W. K., & Emery, B. A. (2004). Direct and Indirect Thermospheric Heating Sources for Solar Cycles 21–23. *Solar Physics*, *224*(1–2), 495–505. https://doi.org/10.1007/s11207-005-6393-4

Knipp, D. J., Eriksson, S., Kilcommons, L., Crowley, G., Lei, J., Hairston, M., & Drake, K. (2011). Extreme Poynting flux in the dayside thermosphere: Examples and statistics: EXTREME DAYSIDE POYNTING FLUX. *Geophysical Research Letters*, *38*(16), n/a-n/a. https://doi.org/10.1029/2011GL048302

Knipp, D. J., Kilcommons, L., Hairston, M., & Coley, W. R. (2021). Hemispheric Asymmetries in Poynting Flux Derived From DMSP Spacecraft. *Geophysical Research Letters*, *48*(17). https://doi.org/10.1029/2021GL094781

Lam, M. M., Freeman, M. P., Jackman, C. M., Rae, I. J., Kalmoni, N. M. E., Sandhu, J. K., & Forsyth, C. (2019). How Well Can We Estimate Pedersen Conductance From the THEMIS White-Light All-Sky Cameras? *Journal of Geophysical Research: Space Physics*, *124*(4), 2920–2934. https://doi.org/10.1029/2018JA026067

Lin, C. S., & Hoffman, R. A. (1982). Observations of inverted-V electron precipitation. *Space Science Reviews*, *33*(4). https://doi.org/10.1007/BF00212420

Lin, D., Wang, W., Merkin, V. G., Huang, C., Oppenheim, M., Sorathia, K., et al. (2022). Origin of Dawnside Subauroral Polarization Streams During Major Geomagnetic Storms. *AGU Advances*, *3*(4), e2022AV000708. https://doi.org/10.1029/2022AV000708

Liu, J., Angelopoulos, V., Chu, X., & McPherron, R. L. (2016). Distribution of Region 1 and 2 currents in the quiet and substorm time plasma sheet from THEMIS observations. *Geophysical Research Letters*, *43*(15), 7813–7821. https://doi.org/10.1002/2016gl069475

Liu, J., Lyons, L. R., Wang, C., Hairston, M. R., Zhang, Y., & Zou, Y. (2020). Dawnside Auroral Polarization Streams. *Journal of Geophysical Research: Space Physics*. https://doi.org/10.1029/2019JA027742

Liu, J., Lyons, L. R., Wang, C., Ma, Y., Strangeway, R. J., Zhang, Y., et al. (2021). Embedded Regions 1 and 2 Field-Aligned Currents: Newly Recognized From Low-Altitude Spacecraft Observations. *Journal of Geophysical Research: Space Physics*, *126*(6). https://doi.org/10.1029/2021JA029207

Liu, J., Higuchi, T., Lyons, L. R., Ohtani, S., Wu, J., Zou, Y., et al. (2022). The Occurrence of Embedded Region 1 and 2 Currents Depends on Geomagnetic Activity Level. *Journal of Geophysical Research: Space Physics*, *127*(11). https://doi.org/10.1029/2022JA030539

Lu, G., Richmond, A. D., Emery, B. A., & Roble, R. G. (1995). Magnetosphere-ionosphere-thermosphere coupling: Effect of neutral winds on energy transfer and field-aligned current. *Journal of Geophysical Research*, *100*(A10), 19643. https://doi.org/10.1029/95JA00766

Lyons, L. R. (1981). Discrete aurora as the direct result of an inferred high-altitude generating potential distribution. *Journal of Geophysical Research*, *86*(A1). https://doi.org/10.1029/JA086iA01p00001

Lysak, R. L. (1985). Auroral electrodynamics with current and voltage generators. *Journal of Geophysical Research*, *90*(A5). https://doi.org/10.1029/JA090iA05p04178

MacDonald, E. A., Donovan, E., Nishimura, Y., Case, N. A., Gillies, D. M., Gallardo-Lacourt, B., et al. (2018). New science in plain sight: Citizen scientists lead to the discovery of optical structure in the upper atmosphere. *Science Advances*, *4*(3), eaaq0030. https://doi.org/10.1126/sciadv.aaq0030

Mozer, F. S., & Hull, A. (2001). Origin and geometry of upward parallel electric fields in the auroral acceleration region. *Journal of Geophysical Research: Space Physics*, *106*(A4), 5763–5778. https://doi.org/10.1029/2000JA900117

Ohtani, S., Kokubun, S., Elphic, R. C., & Russell, C. T. (1988). Field-aligned current signatures in the near-tail region: 1. ISEE observations in the plasma sheet boundary layer. *Journal of Geophysical Research*, *93*(A9), 9709. https://doi.org/10.1029/JA093iA09p09709

Olsson, A., Janhunen, P., Karlsson, T., Ivchenko, N., & Blomberg, L. G. (2004). Statistics of Joule heating in the auroral zone and polar cap using Astrid-2 satellite Poynting flux. *Annales Geophysicae*, *22*(12), 4133–4142. https://doi.org/10.5194/angeo-22-4133-2004

Pakhotin, I. P., Mann, I. R., Xie, K., Burchill, J. K., & Knudsen, D. J. (2021). Northern preference for terrestrial electromagnetic energy input from space weather. *Nature Communications*, *12*(1), 199. https://doi.org/10.1038/s41467-020-20450-3

Panov, E. V., Baumjohann, W., Wolf, R. A., Nakamura, R., Angelopoulos, V., Weygand, J. M., & Kubyshkina, M. V. (2016). Magnetotail energy dissipation during an auroral substorm. *Nature Physics*, *12*(12), 1158–1163. https://doi.org/10.1038/nphys3879

Pearson, K. (1901). LIII. *On lines and planes of closest fit to systems of points in space*. *The London, Edinburgh, and Dublin Philosophical Magazine and Journal of Science*, *2*(11), 559–572. https://doi.org/10.1080/14786440109462720

Qian, C., & Wang, H. (2023). A Statistical Study of Ion Upflow during Periods of Dawnside Auroral Polarization Streams and Subauroral Polarization Streams. *Remote Sensing*, *15*(5), 1320. https://doi.org/10.3390/rs15051320

Rich, F. J. (1984). Fluxgate magnetometer (SSM) for the Defense Meteorological Satellite Program (DMSP) Block 5D-2, flight 7. Tech. Rep. AFGL-TR-84-0225, Air Force Geophys. Lab., Hanscom Air Force Base, Mass.

Robinson, R. M., Vondrak, R. R., Miller, K., Dabbs, T., & Hardy, D. (1987). On calculating ionospheric conductances from the flux and energy of precipitating electrons. *Journal of Geophysical Research: Space Physics*, *92*(A3), 2565–2569. https://doi.org/10.1029/JA092iA03p02565

Schunk, R. W., & Sojka, J. J. (1996). Ionosphere-thermosphere space weather issues. *Journal of Atmospheric and Terrestrial Physics*, *58*(14), 1527–1574. https://doi.org/10.1016/0021-9169(96)00029-3

Tanaka, T. (1995). Generation mechanisms for magnetosphere-ionosphere current systems deduced from a three-dimensional MHD simulation of the solar wind-magnetosphere-ionosphere coupling processes. *Journal of Geophysical Research*, *100*(A7), 12057. https://doi.org/10.1029/95JA00419

Vickrey, J. F., Vondrak, R. R., & Matthews, S. J. (1982). Energy deposition by precipitating particles and Joule dissipation in the auroral ionosphere. *Journal of Geophysical Research: Space Physics*, *87*(A7), 5184–5196. https://doi.org/10.1029/JA087iA07p05184

Vickrey, J. F., Livingston, R. C., Walker, N. B., Potemra, T. A., Heelis, R. A., Kelley, M. C., & Rich, F. J. (1986). On the current-voltage relationship of the magnetospheric generator at intermediate spatial scales. *Geophysical Research Letters*, *13*(6), 495–498. https://doi.org/10.1029/GL013i006p00495

Voiculescu, M., & Roth, M. (2008). Eastward sub-auroral ion drifts or ASAID. *Annales Geophysicae*, *26*(7), 1955–1963. https://doi.org/10.5194/angeo-26-1955-2008

Walach, M. -T., Grocott, A., Thomas, E. G., & Staples, F. (2022). Dusk-Dawn Asymmetries in SuperDARN Convection Maps. *Journal of Geophysical Research: Space Physics*, *127*(12), e2022JA030906. https://doi.org/10.1029/2022JA030906

Wang, H., Ridley, A. J., Lühr, H., Liemohn, M. W., & Ma, S. Y. (2008). Statistical study of the subauroral polarization stream: Its dependence on the cross–polar cap potential and subauroral conductance. *Journal of Geophysical Research: Space Physics*, *113*(A12), 2008JA013529. https://doi.org/10.1029/2008JA013529

Wang, H., Lühr, H., Häusler, K., & Ritter, P. (2011). Effect of subauroral polarization streams on the thermosphere: A statistical study: STUDY OF SAPS EFFECT ON THERMOSPHERE. *Journal of Geophysical Research: Space Physics*, *116*(A3). https://doi.org/10.1029/2010JA016236

Wiltberger, M., Wang, W., Burns, A. G., Solomon, S. C., Lyon, J. G., & Goodrich, C. C. (2004). Initial results from the coupled magnetosphere ionosphere thermosphere model: magnetospheric and ionospheric responses. *Journal of Atmospheric and Solar-Terrestrial Physics*, *66*(15–16), 1411–1423. https://doi.org/10.1016/j.jastp.2004.03.026

Wygant, J. R., Keiling, A., Cattell, C. A., Johnson, M., Lysak, R. L., Temerin, M., et al. (2000). Polar spacecraft based comparisons of intense electric fields and Poynting flux near and within the plasma sheet-tail lobe boundary to UVI images: An energy source for the aurora. *Journal of Geophysical Research: Space Physics*, *105*(A8), 18675–18692. https://doi.org/10.1029/1999ja900500

Zhang, Q., Liu, Y. C. -M., Zhang, Q. -H., Xing, Z., Wang, Y., & Ma, Y. (2020). Statistical Study of Ion Upflow Associated with Subauroral Polarization Streams (SAPS) at Substorm Time. *Journal of Geophysical Research: Space Physics*, *125*(3), e2019JA027163. https://doi.org/10.1029/2019JA027163

Zou, S., Moldwin, M. B., Nicolls, M. J., Ridley, A. J., Coster, A. J., Yizengaw, E., et al. (2013). Electrodynamics of the high-latitude trough: Its relationship with convection flows and field-aligned currents. *Journal of Geophysical Research: Space Physics*, *118*(5), 2565–2572. https://doi.org/10.1002/jgra.50120

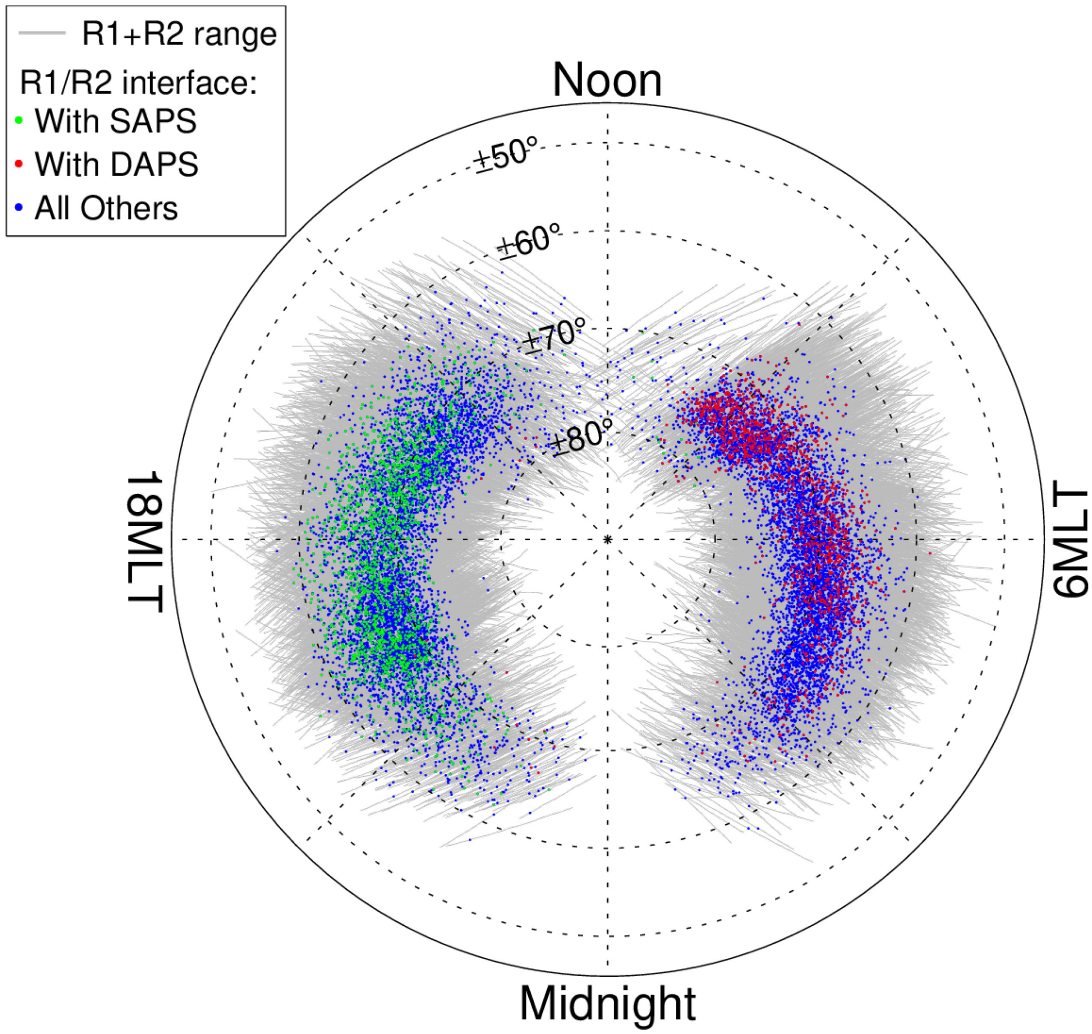

Fig. 1. The locations of the observations used in our statistical study. Grids: magnetic latitude and MLTs. Gray lines: Defense Meteorological Satellite Program trajectories in the latitudinal range covered by R1 and R2 currents. Green, red, and blue dots: R1/R2 interface locations for transects identified to contain DAPS, those containing SAPS, and all other ones, respectively. Please note that the dots do not indicate the exact locations of SAPS or DAPS.

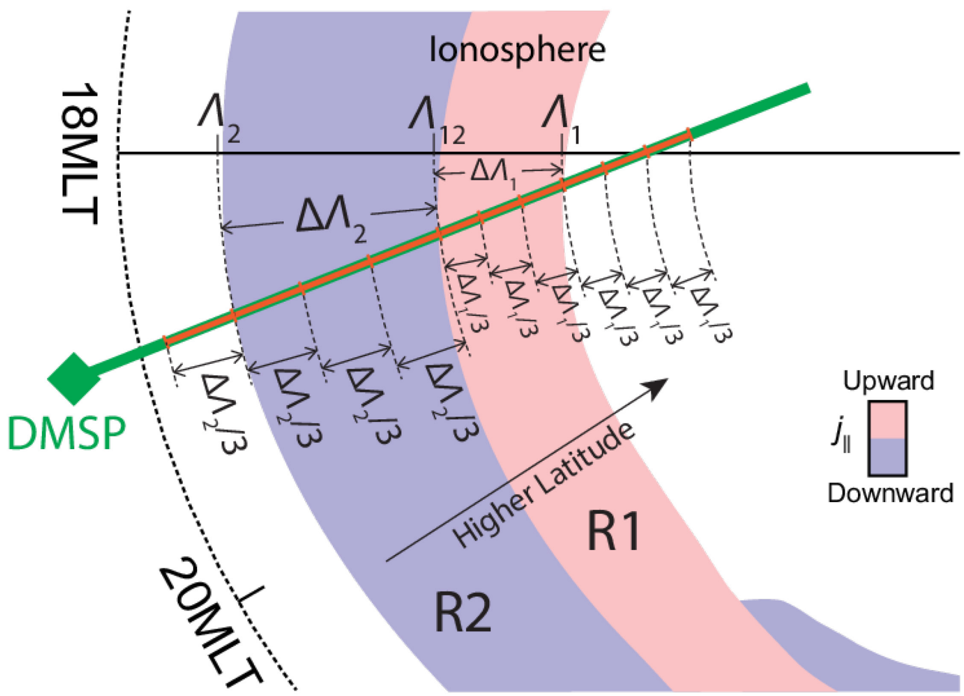

Fig. 2. A Schematic illustration of how we segment a DMSP transect of the Region 1 and 2 currents in the ionosphere. Pink/light blue: upward/downward field-aligned currents. Green line and diamond: schematic track of a DMSP spacecraft. Each dashed curve is of a constant magnetic latitude. Λ_1, Λ_2, and Λ_{12} are the magnetic latitudes of the poleward boundary of the R1 current, the equatorward boundary of the R2 current, and the R1/R2 interface, respectively. $\Delta\Lambda_1$ and $\Delta\Lambda_2$ are the widths of the R1 and R2 currents in magnetic latitude, respectively. From these values we determine the orange segments for computing average values (see Section 3).

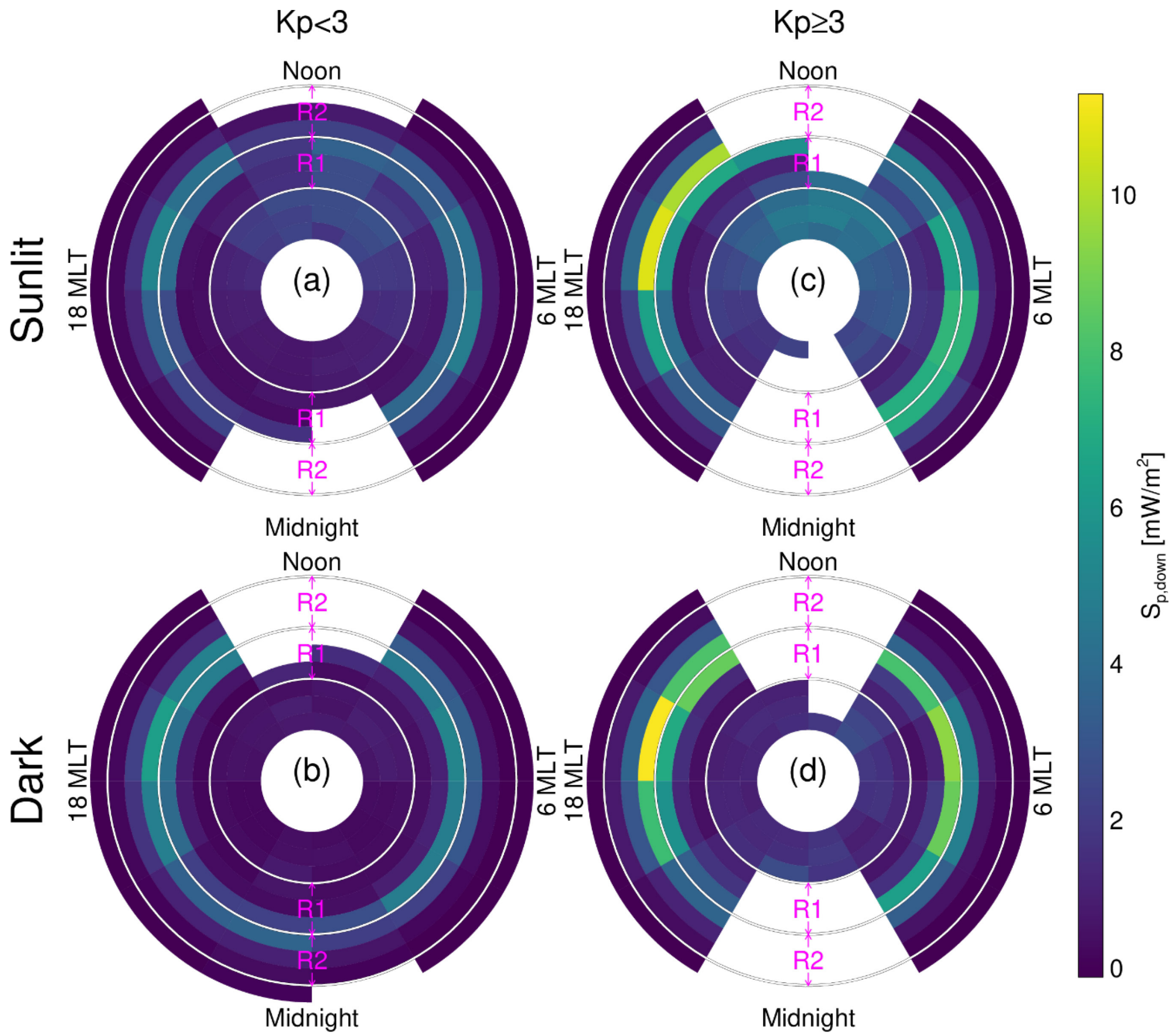

Fig. 3. Statistical distribution of typical S_p at various locations around the auroral zone under (a-b) quiet, (c-d) active, (a, c) sunlit, and (b, d) dark conditions, as reconstructed from DMSP transects of the auroral zone (including both northern and southern hemispheres). Color of each bin: the median of the signature S_p values of all spacecraft trajectory segments falling inside that bin (see Section 3; the lower and upper quartiles of the values are illustrated in Figures S1 and S2 of the supporting information, respectively). A positive S_p means a Poynting flux downwards towards the ground. White circles from small to large: the poleward boundary of the R1 current, the R1/R2

interface, and the equatorward boundary of the R2 current. For each panel, the center of the circles is the magnetic pole; a radially increasing distance from the center represents a decreasing normalized magnetic latitude (normalized by the R1 or R2 current's latitudinal width). Each bin's normalized latitudinal width is 1/3; it has been normalized by the latitudinal width of the R1 (R2) current if it is poleward (equatorward) of the R1/R2 interface.

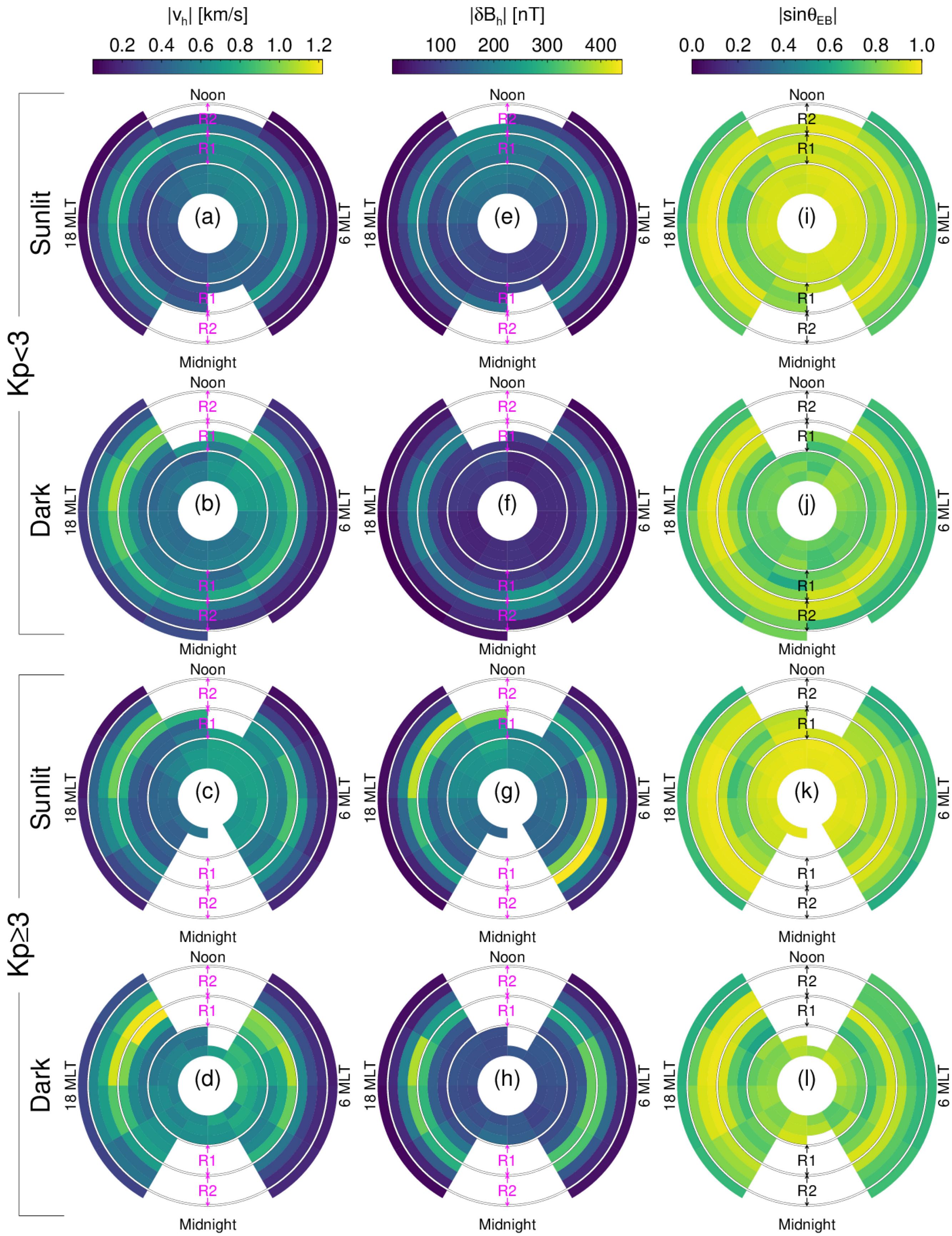

|v_h| [km/s]
0.2 0.4 0.6 0.8 1.0 1.2
|δB_h| [nT]
100 200 300 400
|sinθ_EB|
0.0 0.2 0.4 0.6 0.8 1.0
Kp<3
Kp≥3
Sunlit
Dark
Noon
Midnight
18 MLT
6 MLT
R1
R2
(a)
(b)
(c)
(d)
(e)
(f)
(g)
(h)
(i)
(j)
(k)
(l)

711

Fig. 4. Distributions of (a-d) horizontal ion bulk speed, (e-h) horizontal perturbation magnetic field strength, and (i-l) the sine function of the angle between the horizontal electric field and the horizontal perturbation magnetic field under (a-b, e-f, i-j) quiet, (c-d, g-h, k-l) active, (a, e, I, c, g, k) sunlit, and (b, f, j, d, h, l) dark conditions. Each panel is presented in the same way as those in Figure 3.

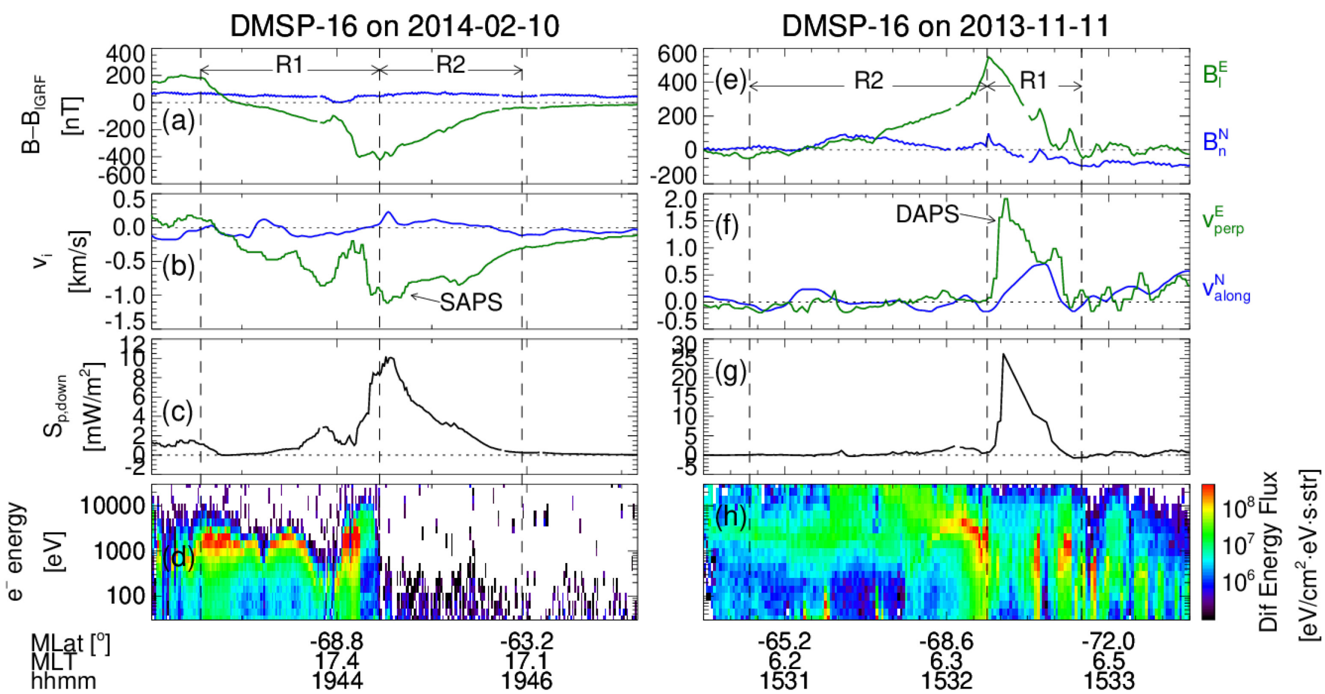

Fig. 5. Examples of (a-d) SAPS and (e-h) DAPS observations. (a, d) Horizontal perturbation magnetic field. Blue (green) component: in the minimum (maximum) variance direction; positive when approximately northward (eastward). We obtain these directions by applying a principal axis analysis (Pearson, 1901) to the interval of R1 and R2 currents. (b, e) Horizontal ion bulk velocity parallel and perpendicular to the spacecraft trajectory, as illustrated by the blue and green curves, respectively. The blue (green) component is positive when approximately northward (eastward). (c, f) Perturbation Poynting flux. (d, g) Differential energy flux of electron precipitation.

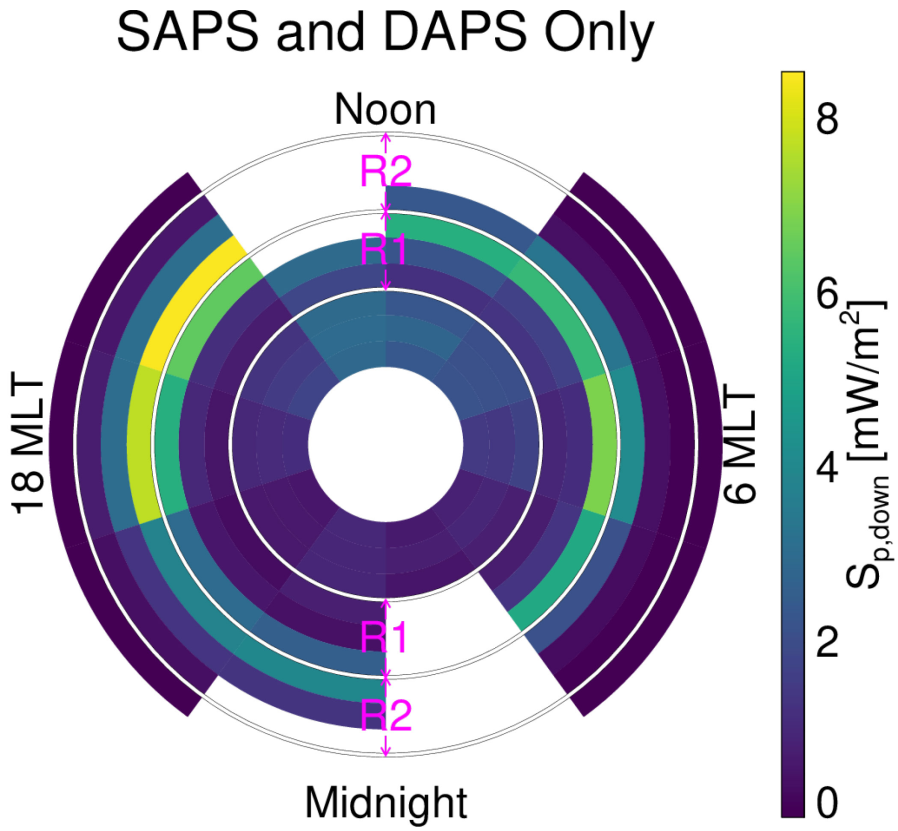

Fig. 6. A statistical distribution of median S_p reconstructed from DMSP transects containing either SAPS or DAPS, presented in the same format as Figure 3. The corresponding lower and upper quartiles are illustrated in Figures S3 and S4 of the supporting information, respectively.

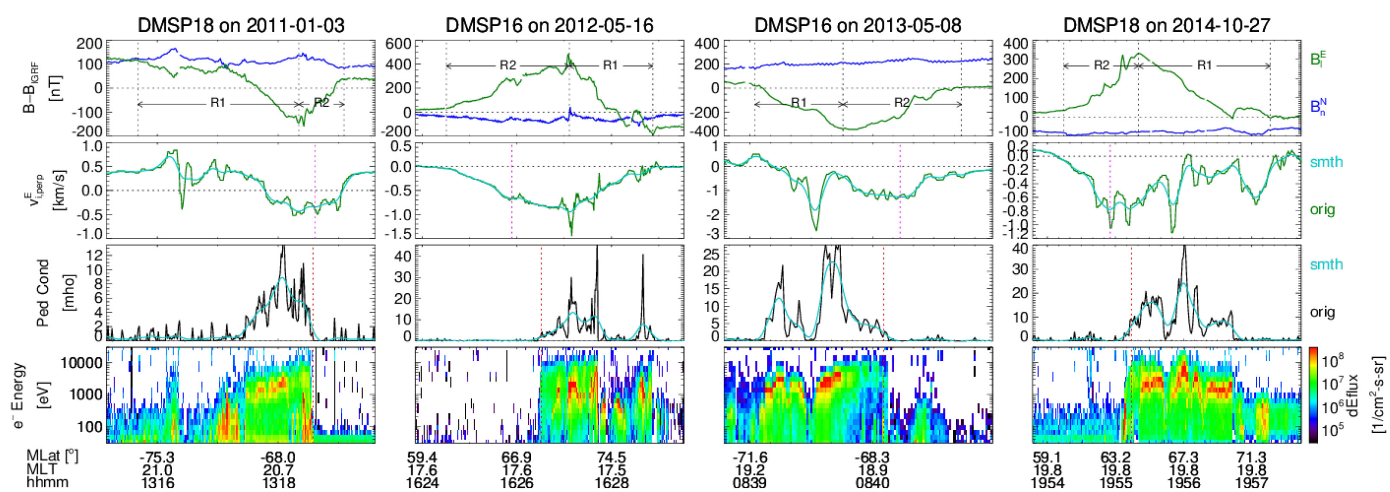

Fig. A1. Examples of SAPS identified by our selection algorithm. The top and bottom rows present the same quantities as Figures 5a and 5d, respectively. Second row from top: Horizontal ion bulk velocity perpendicular to the spacecraft trajectory, positive when approximately eastward. The green and cyan curves are original and smoothed data (see Appendix A for the smoothing technique), respectively. The dotted magenta lines indicate the peaks of the identified SAPS. Third row from top: Pederson conductance computed from the Robinson (1987) equation. The blue and cyan curves are the original and smoothed data, respectively. The dotted orange lines indicate the equatorward boundaries of the electron aurora as determined by our algorithm.

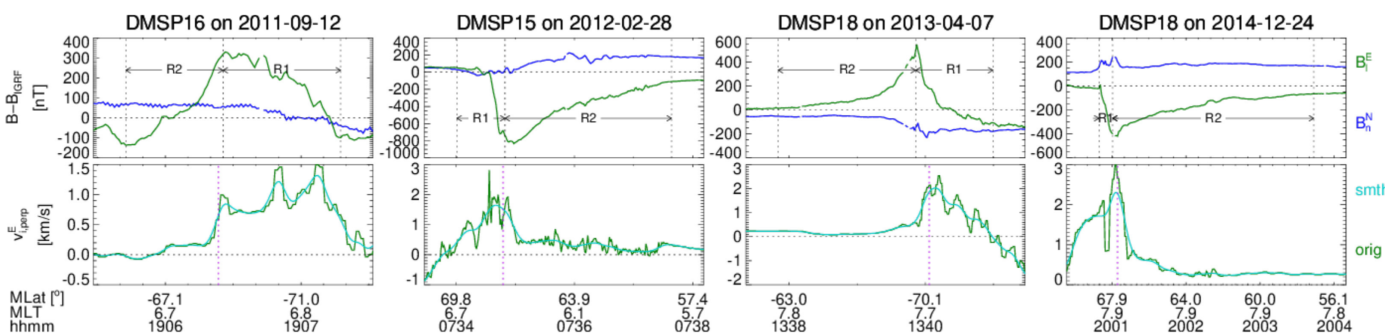

Fig. A2. Examples of DAPS identified by our selection algorithm. The panels present the same quantities as those in the first two rows of Figure A1. Magenta dotted lines indicate DAPS (marked at the poleward edge of the significant gradients of the smoothed flow; see Appendix A.2).